J. Ocean Univ. China (Oceanic and Coastal Sea Research)
https://doi.org/10.1007/s11802-019-3966-7
ISSN 1672-5182, 2019 18 (4): 761-770
http://www.ouc.edu.cn/xbywb/
E-mail:xbywb@ouc.edu.cn

Internal Tide Generation and Dissipation by Small Periodic Topography in Deep Ocean

LI Qiang[1), 2)], MAO Xianzhong[1)], DENG Guotong[1)], ZHAO Ruixiang[2)], ZHANG Chuanzheng[2)], and ZHU Xiaohua[2), *]

1) *Graduate School at Shenzhen*, *Tsinghua University*, *Shenzhen* 518055, *China*
2) *State Key Laboratory of Satellite Ocean Environment Dynamics*, *Second Institute of Oceanography*, *Ministry of Natural Resources*, *Hangzhou* 310012, *China*

(Received July 18, 2018; revised August 7, 2018; accepted August 17, 2018)

Abstract Internal tides generated by a rough sea floor are an important source of mixing in the abyssal ocean. Two linear models are employed to evaluate the conversion rate from barotropic tides to internal tides and the energy distribution in each mode. Considering the periodicity of internal tides, the topography is represented by periodically distributed knife edges and sinusoidal ridges within one wavelength of mode-1 internal tides. The knife edges generate greater internal tides than the sinusoidal ridges due to their sharp shape, which approximates an extremely supercritical condition. Energy flux concentrates in modes whose numbers are multiples of the knife edge or ridge number. Then, a fully nonlinear model that integrates viscosity and diffusion is implemented, and its results are compared with those of the linear model. Internal wave rays generated in the nonlinear model show a distribution similar to the linear models' prediction. High dissipation rates coincide with the rays, suggesting that nonlinear wave-wave interaction is a dominant mechanism for internal tide dissipation in the abyssal ocean.

Key words internal wave generation; multiple ridges; normal modes; conversion rate; dissipation

1 Introduction

In a stratified ocean, interaction between barotropic tides and rough topography generates internal tides. Approximately 1 TW energy is estimated to be lost from barotropic tides through conversion to internal tides in the deep ocean (St. Laurent and Garrett, 2002). As a result of instability, nonlinear processes, and interactions with topography, internal tide energy cascades into instability and turbulence (Sarkar and Scotti, 2017). Their dissipation provides half of the energy input to global diapycnal mixing, which maintains oceanic stratification and overturning circulation (Garrett, 2003). However, many open questions still exist with regard to the entire process of internal tide generation, evolution and dissipation. The relationship between internal tide energy loss and sea floor roughness in particular is still not thoroughly known, although observations have already revealed a direct connection between them (Polzin *et al.*, 1997).

The conversion rate from barotropic tides to internal tides is given by a series of linear analytical models. The topographic steepness parameter ε, which is a slope ratio between topography and internal wave characteristics, is an important factor for internal tide generation. The efficiency of internal tide generation is improved considerably if critical or supercritical conditions ($\varepsilon \geq 1$) exist. The first analytical formula for the conversion rate was provided by Bell (1975) for subcritical ($\varepsilon < 1$) and small topography in infinitely deep water and is proportional to the power spectrum of the topography. For a special case with sinusoidal topography, the conversion rate is proportional to the square of topographic height. Pétrélis *et al.* (2006) extended the calculation of conversion rates to supercritical conditions ($\varepsilon > 1$) for an isolated submarine ridge. St. Laurent *et al.* (2003) used knife edges and top hat-like ridges to represent the topography; these edges and ridges are not continuously differentiable but can be treated as limit cases of supercritical topography. Constructive and destructive interference of internal tides generated from different ridges can change the conversion rates considerably (Balmforth and Peacock, 2009; Kelly and Nash, 2010; Klymak *et al.*, 2013). Relevant evidence is found in Luzon Strait, where semidiurnal internal tide generation is enhanced while diurnal generation is reduced because the separation between the two ridges in Luzon Strait is approximately one wavelength of semidiurnal internal tides.

Local mixing is mainly sustained by the dissipation of high-mode internal waves generated from small topographic features through nonlinear wave-wave interaction (Polzin, 2004, 2009; Nikurashin and Legg, 2011) or con-

* Corresponding author. E-mail: xhzhu@sio.org.cn

vective and shear instability (Muller and Bühler, 2009). Low-mode internal tides escape from their generation sites due to their long wavelengths. St. Laurent and Garrett (2002) estimated that about 30% of generated internal tides dissipate locally, while recent observations and theoretical estimates suggest that this fraction depends on local forcing and Coriolis frequency (Klymak *et al.*, 2013). This fraction estimate is especially important for the oceanographic community, because it provides a basis for tidal mixing parameterization in climate models.

Several hot spots are usually present on a rough sea floor for internal tide generation. Interference of internal tides, which come from different generation sites, may enhance or reduce the total conversion from barotropic to internal tides. In this paper, we intend to demonstrate the whole process of internal tide generation by periodic ridges and their evolution and dissipation above. Considering the periodicity of internal tides, the ridges are evenly distributed within one wavelength of mode-1 internal tides. Parameter space that corresponds to our model configurations is first analyzed in Section 2 to clarify how important the nonlinear effects are and which instability may be triggered during internal tide generation. In Section 3, two simplified linear models are applied with two types of idealized topography: knife edge and sinusoidal ridges. In Section 4, the results from the linear models are compared with those of a fully nonlinear numerical model to demonstrate the internal tide dissipation related to nonlinear effects, viscosity, and diffusion. Conclusions are presented in Section 5.

2 Parameter Space

Here, we consider internal tide generation by rough bathymetry in a deep ocean. The topographic height h is presumed to be much less than the total water depth H. Internal tide generation by abrupt ridges or a shelf break is not within the scope of this paper. Six parameters determine internal tide generation: the tidal frequency ω, the Coriolis frequency f, the buoyancy frequency N, the topographic height h, the topographic wavenumber k, and the magnitude of barotropic tidal flow U_0 (Garrett and Kunze, 2007). Aside from the topographic height parameter $\delta = h/H$, internal tide generation is also related to two other important nondimensional parameters. One is the excursion number

$$\mu = \frac{U_0 k}{\omega}, \tag{1}$$

which is a ratio of net advection by barotropic tides to the topographic length scale. If $\mu << 1$, then the generated internal tides are nearly symmetric at all phases. If $\mu > 1$, then lee waves will be generated during the high-velocity state and then released when the tidal flow slackens (Sarkar and Scotti, 2017). The other one is the steepness parameter

$$\varepsilon = \frac{h_x}{\alpha}, \tag{2}$$

in which h_x is the gradient of the topography and

$$\alpha = \sqrt{\frac{\omega^2 - f^2}{N^2 - \omega^2}} \tag{3}$$

is the slope of internal wave characteristics. Internal tide generation is efficient if the topography is critical ($\varepsilon = 1$) or supercritical ($\varepsilon > 1$). Internal wave beams are emitted from the critical slope, related to energetic high-mode internal waves. Here we assume that the topography is sinusoidal and take the hydrostatic and non-rotational approximations so that

$$\varepsilon = \frac{kNh_0}{\omega}. \tag{4}$$

Internal tides play an important role in abyssal mixing either by causing turbulence due to instability or breaking small-scale waves due to nonlinear interaction. In the scale analysis, we use the amplitude U_0 of the barotropic tidal flow to represent the velocity scale of internal tides. Specifically for internal tides, the Richardson number can be written as

$$Ri = O\left(\frac{N^2}{u_z^2}\right) = \left(\frac{\omega}{k_n U_0}\right)^2, \tag{5}$$

where k_n is the wavenumber of mode-n mode internal tides. The Richardson number $Ri < 0.25$ is a necessary condition for shear instability. The Froude number

$$Fr_n = \frac{U_0}{c_n} = \frac{k_n U_0}{\omega} \tag{6}$$

is usually used to measure the nonlinear wave-wave interaction, which is equal to $Ri^{-1/2}$ for internal tides.

Garrett and Kunze (2007) proposed the conditions for linearization in the ε-μ plane (Fig.1). One linear regime is in $\varepsilon\mu << 1$, and the other one requires large U_0/Nh_0 for

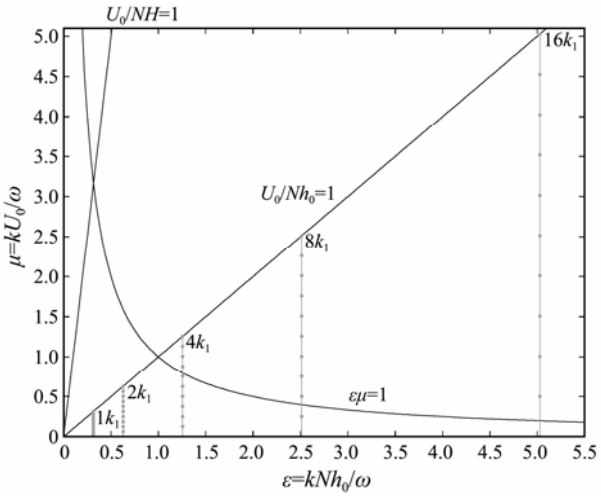

Fig.1 Parameter space of internal tide generation. Gray dot lines indicate the parameters used in this paper for 1, 2, 4, 8, and 16 sinusoidal ridges with different tidal forcing U_0 = 0, 0.1, 0.2, ···, 1.0 m s^{-1} (dots).

large excursion. However, to avoid nonlinear wave-wave interaction, a requirement is that $Fr<<1$, thereby further reducing the latter linear regime. In our following analysis, $N=0.005\,\mathrm{s}^{-1}$, $h=100\,\mathrm{m}$, and $H=1000\,\mathrm{m}$. Their locations in the parameter space are shown as gray lines and dots in Fig.1 for varied ridge separation and U_0.

3 Linear Internal Tide Generation

Given the periodicity of internal tides, we consider the internal tide generation by small Periodic topography within one wavelength λ_1 of mode-1 internal tides. The topography is characterized using the topographic wavenumber k, which is selected to be multiples of the wavenumber k_1 of mode-1 internal tides so that we can establish a relationship between internal tide generation and rough topography in a perspective of the Fourier transform. In this section, we will use two linear analytical models with the topography represented by knife edges and by sinusoidal ridges. Detailed model parameters are shown in Table 1.

Table 1 Parameters in the linear models

Parameter	Notation	Value
Tidal frequency (M_2)	ω	$1.4\times10^{-4}\,\mathrm{s}^{-1}$
Buoyancy frequency	N	$5.0\times10^{-3}\,\mathrm{s}^{-1}$
Coriolis frequency	f	0
Ridge height	h_0	100 m
Total depth	H	1000 m
Viscosity	v	0

3.1 Knife Edge Model

The topography is represented by multiple knife edges that are evenly distributed in one wavelength of mode-1 internal tides

$$h=\begin{cases}h_0 & \text{if } x=x^{(j)} \text{ for } j=1,2,...,N_r\\ 0 & \text{otherwise}\end{cases}. \tag{7}$$

The internal wave velocities (u, w) on each side of the knife edge are written in a composition of normal modes

$$\begin{cases}u^{(j)}=U_0+\sum_{n=1}^{\infty}\left\{a_n^{(j)}\mathrm{e}^{ik_n^{(j)}x^{(j)}}\phi_n+b_n^{(j)}\mathrm{e}^{-ik_n^{(j)}x^{(j)}}\phi_n\right\}\\ u^{(j+1)}=U_0+\sum_{n=1}^{\infty}\left\{a_n^{(j+1)}\mathrm{e}^{ik_n^{(j+1)}x^{(j)}}\phi_n+b_n^{(j+1)}\mathrm{e}^{-ik_n^{(j+1)}x^{(j)}}\phi_n\right\}\\ w^{(j)}=\sum_{n=1}^{\infty}\left\{-a_n^{(j)}ik_n^{(j)}\mathrm{e}^{ik_n^{(j)}x^{(j)}}\phi_{wn}+b_n^{(j)}ik_n^{(j)}\mathrm{e}^{-ik_n^{(j)}x^{(j)}}\phi_{wn}\right\},\\ w^{(j+1)}=\sum_{n=1}^{\infty}\left\{-a_n^{(j+1)}ik_n^{(j+1)}e^{ik_n^{(j+1)}x^{(j)}}\phi_{wn}+\right.\\ \qquad\left.b_n^{(j+1)}ik_n^{(j+1)}e^{-ik_n^{(j+1)}x^{(j)}}\phi_{wn}\right\}\end{cases} \tag{8}$$

where ϕ_n and ϕ_{wn} are the vertical structure function for u and w of mode-n internal waves, respectively. a_n and b_n are the amplitude of mode-n internal waves propagating in the $\pm x$ direction, respectively (Fig.2). Through matching the velocity at each knife edge, *i.e.*,

$$\begin{cases}u^{(j)}=u^{(j+1)} & -H<z<0\\ u^{(j)}=u^{(j+1)}=0 & -H<z<-H+h_0\\ w^{(j)}=w^{(j+1)} & -H+h_0<z<0\end{cases}, \tag{9}$$

and also considering the orthogonality of normal modes, we obtain the following equations written in a matrix format:

$$\begin{cases}\boldsymbol{U}^{(j)}\boldsymbol{a}^{(j)}+\boldsymbol{U}^{*(j)}\boldsymbol{b}^{(j)}-\boldsymbol{U}^{(j)}\boldsymbol{a}^{(j+1)}-\boldsymbol{U}^{*(j)}\boldsymbol{b}^{(j+1)}=0\\ (\boldsymbol{P}^{(j)}+\boldsymbol{W}^{(j)})\boldsymbol{a}^{(j)}+(\boldsymbol{P}^{*(j)}-\boldsymbol{W}^{*(j)})\boldsymbol{b}^{(j)}-\\ \qquad\boldsymbol{W}^{(j)}\boldsymbol{a}^{(j+1)}+\boldsymbol{W}^{*(j)}\boldsymbol{b}^{(j+1)}=\boldsymbol{U}_0^{(j)}\end{cases}. \tag{10}$$

Here, * represents the conjugate, and the matrix elements are

$$\begin{cases}U_{n,n}^{(j)}=\mathrm{e}^{ik_nx^{(j)}}\\ P_{m,n}^{(j)}=\mathrm{e}^{ik_nx^{(j)}}\int_{-H}^{-H_s}\phi_n\phi_m\mathrm{d}z\\ W_{m,n}^{(j)}=k_n^{(j)}\,\mathrm{e}^{ik_nx^{(j)}}\int_{-H_s}^{0}\phi_{wn}\phi_m\mathrm{d}z\\ U_{0m}^{(j)}=-U_0\int_{-H}^{-H_s}\phi_m\mathrm{d}z\end{cases}. \tag{11}$$

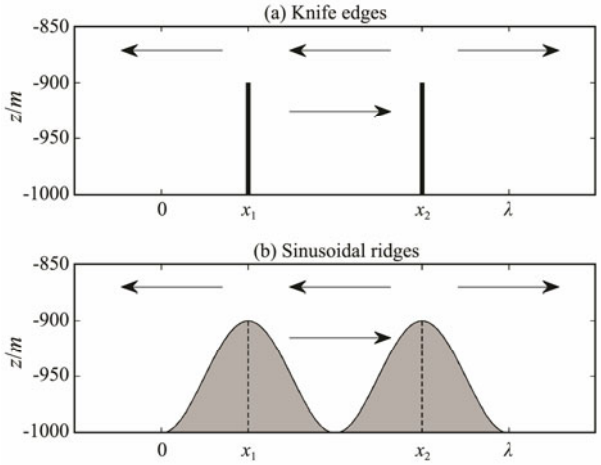

Fig.2 Schematics of internal tide generation model with knife edges (top) and sinusoidal ridges (bottom). Arrows indicate the propagation of generated internal tides.

Given that no incident internal waves exist, $a^{(1)}$ and $b^{(Nr+1)}$ are known to be zero. Thus, the amplitudes $\boldsymbol{a}^{(j)}$ and $\boldsymbol{b}^{(j)}$ of generated internal tides are obtained through an inversion of a series of linear Eq. (10) (St. Laurent *et al.*, 2003; Kelly *et al.*, 2013). The energy fluxes of eastward- and westward-propagating internal tides are

$$J^{(T)}=\sum_{n=1}^{\infty}\frac{1}{2}\rho_0c_nHa_na_n^* \quad\text{and}\quad J^{(R)}=\sum_{n=1}^{\infty}\frac{1}{2}\rho_0c_nHb_nb_n^*, \tag{12}$$

respectively. Here, * represents the conjugation. Fig.3 shows wave field u for internal tide generation by 1, 2, 10,

and 16 knife edges, respectively. Four internal wave beams are emitted from the peak of each knife edge. Two propagate upwards and the other two propagate downwards along their characteristic slope α.

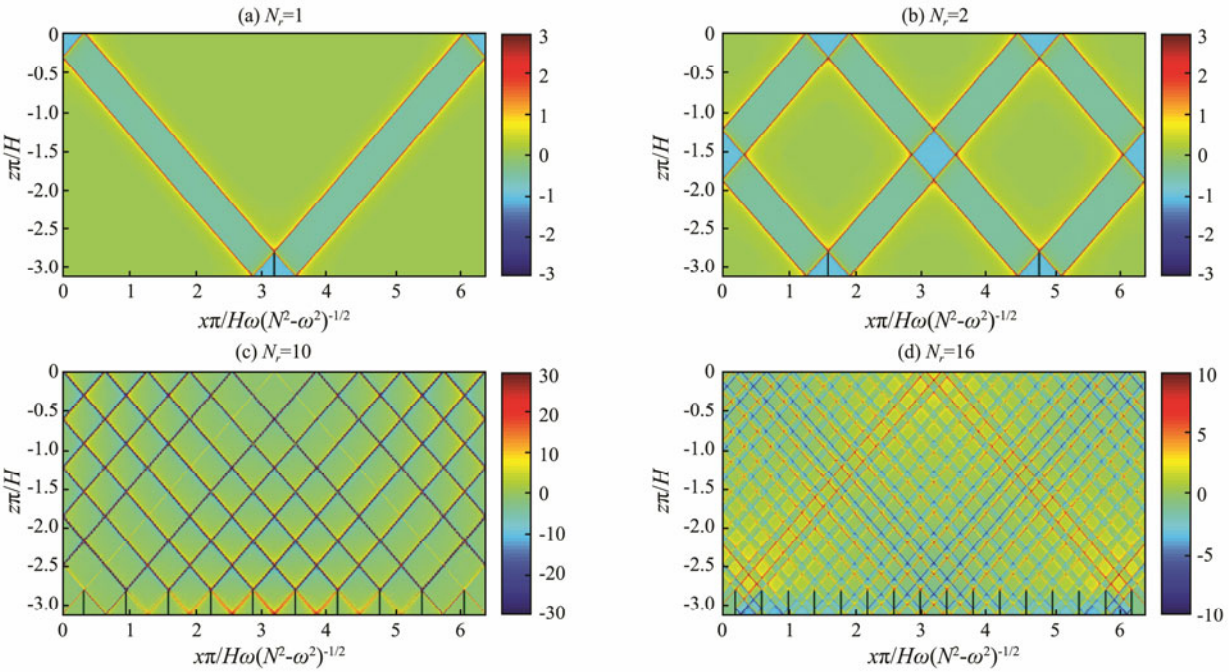

Fig.3 Wavefields u show internal tide generation by 1, 2, 10, and 16 knife edges.

3.2 Sinusoidal Ridges

We extend the topography from knife edges to sinusoidal topography represented by

$$h = h_0\left[1-\sin(N_r k_1 x)\right],\ 0 \le x \le \lambda_1 . \tag{13}$$

Then, the internal tide generation problem is solved using the iTides software developed at MIT (http://sourceforge.net/projects/itides/), which solves the internal wave equation using the Green's function method by treating the bottom boundary as a series of singularity points (Balmforth and Peacock, 2009; Echeverri and Peacock, 2010). The model parameters are same as those of the knife edge model (Table 1). The bottom slope is subcritical ($\varepsilon<1$) for the cases with 1 and 2 ridges; therefore, no obvious beams radiate from the ridges. Fig.4 shows wave field u for internal tide generation by 8, 11, 15, and 16 sinusoidal ridges. For the case with 8 ridges (Fig.4a), the beam that is emitted from the west flank of the western-

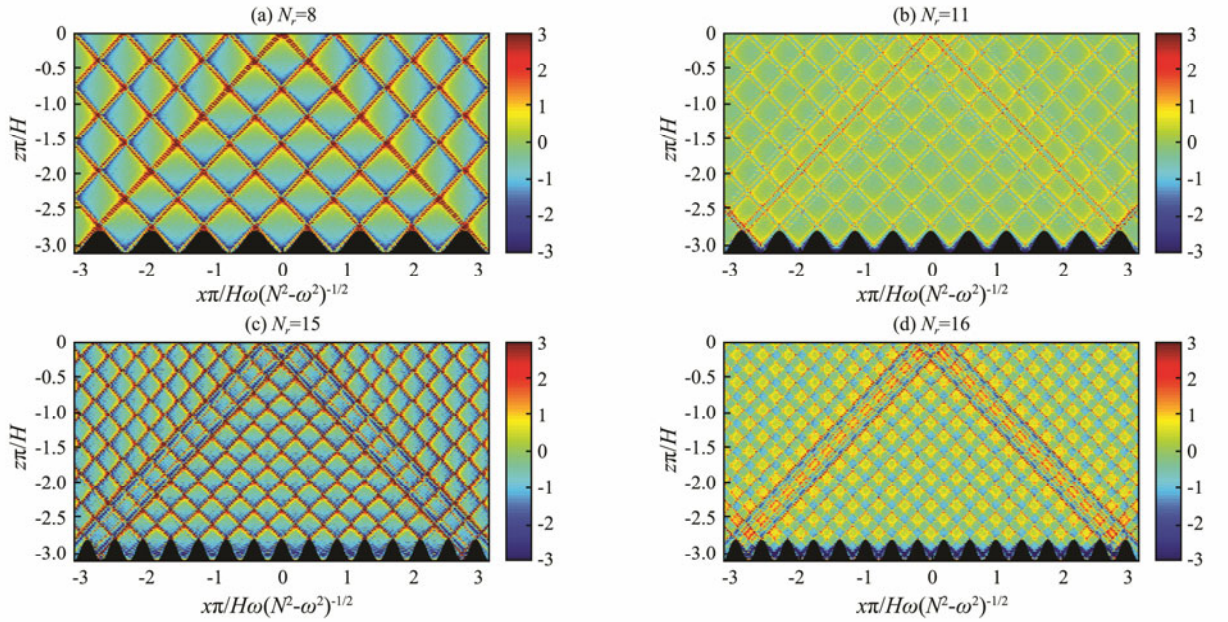

Fig.4 Wavefields u show internal tide generation by 8, 11, 15, and 16 sinusoidal ridges.

most ridge and is then reflected from the surface is coincident with the beam emitted from the east flank of the easternmost ridge. This constructive beam interference markedly enhances the internal tide generation (Balmforth and Peacock 2009).

3.3 Energy Flux and Conversion

The knife edge model and the Green's function method are based on the linearity assumption. However, the energy flux of generated internal tides, *i.e.*, the barotropic to baroclinic conversion rate, is not a linear sum of the rates for each ridge. Its variation is related to constructive or destructive interference of rays (Balmforth and Peacock, 2009; Klymak *et al.*, 2013).

For the knife edge model (Fig.5), the average energy flux by each knife edge reaches its maximum with 10 knife edges. In this case, the downward propagating ray from the peak of one knife edge, after its reflection from the bottom, is coincidently overlapped with the upward-propagating ray emitted from the peak of the neighbor knife edge (Fig.3c). The interference is in phase, thereby enhancing the internal tide generation. In Fig.3d (N_r=16), the downward propagating ray is bounced back after two reflections from the bottom and the neighbor knife edge. This ray is out-of-phase with the upward-propagating ray emitted from the same knife edge. Therefore, the internal tide generation is reduced.

Ray interference is more complicated for sinusoidal ridges due to multiple reflections and critical slopes. The downward propagating ray will move upwards after reflection if it reaches a subcritical slope (Figs.6a and 6b). Otherwise, it will move downwards if it reaches a supercritical slope (Figs.6c and 6d). After one or several reflections, the ray will escape from the trough between ridges. Depending on its interference with the upward-propagating ray directly emitted from the ridge, internal tide generation will be enhanced or reduced. For example, in Figs.6a and 6c, the reflected rays are in phase with the ray generated from the neighbor ridge; the average energy flux by ridge reaches its maximum, as shown in Fig.7; and out-of-phase interference corresponds to the minimum energy flux.

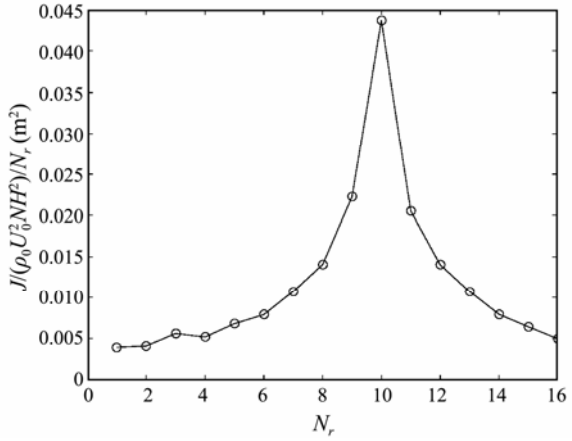

Fig.5 Average conversion rate by each knife edge.

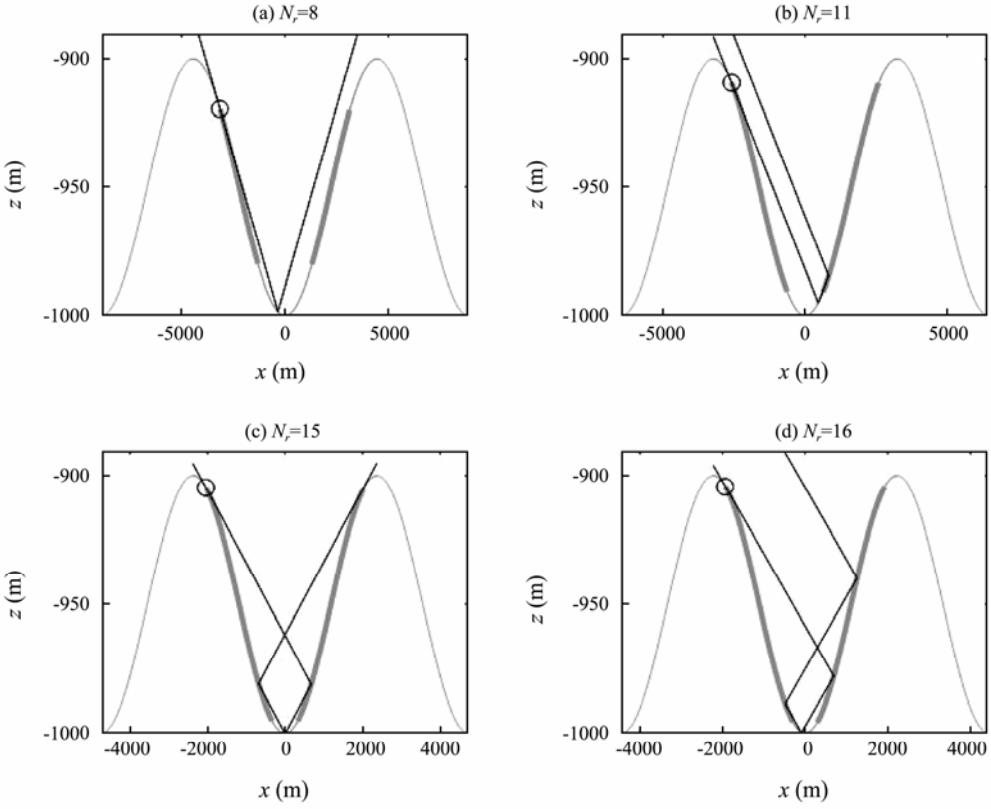

Fig.6 Ray tracing (black lines) for sinusoidal ridges. Thin gray lines represent the sinusoidal ridges, and thick gray lines represent supercritical slopes. Black circles are the critical point where the ray originates.

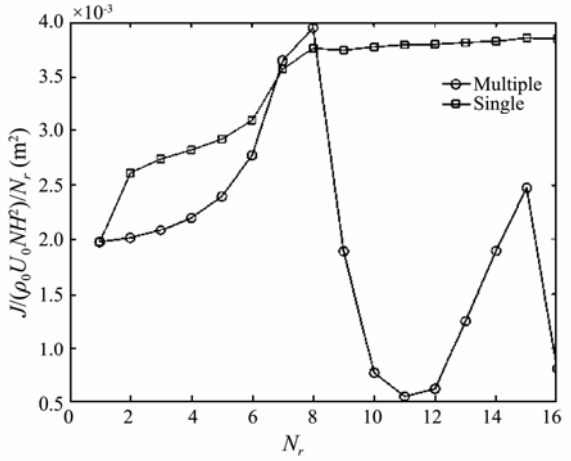

Fig.7 Average conversion rate by each sinusoidal ridge, solved using the Green's function method. Black circles denote multiple ridges, and gray squares indicate a single ridge with the same shape as the multiple-ridge case.

The distribution of energy flux in each mode shows a direct relationship with the ridge number N_r. The energy flux of generated internal tides concentrates on the modes whose numbers are integer multiples of N_r (Fig.8). This energy flux distribution is probably related to the forcing term on the right-hand side of the internal tide generation equation (Garrett and Gerkema, 2007)

$$\varphi_{xx}-\frac{\omega^2-f^2}{N^2-\omega^2}\varphi_{zz}=\frac{N^2}{N^2-\omega^2}U_0 z\left(\frac{H}{H-h}\right)_{xx}. \quad (14)$$

Its Fourier transform is

$$-k^2\hat{\varphi}-\frac{\omega^2-f^2}{N^2-\omega^2}\hat{\varphi}_{zz}=-k^2\frac{N^2}{N^2-\omega^2}U_0 z\cdot\left(\frac{H}{H-h}\right). \quad (15)$$

The top hat represents the Fourier transform with x. For sinusoidal topography,

$$h(x)=h_0\sin(N_r k_1 x), \quad (16)$$

the Fourier transform of $H/(H-h)$ reveals peak values at integer multiples of $N_r k_1$. We do not have an analytical expression of it so far. According to the calculation using the Green's function method, this phenomenon is more obvious for small topography ($h<<H$). This condition implies that only high-mode internal waves can be generated in the deep ocean if the wavenumber of rough

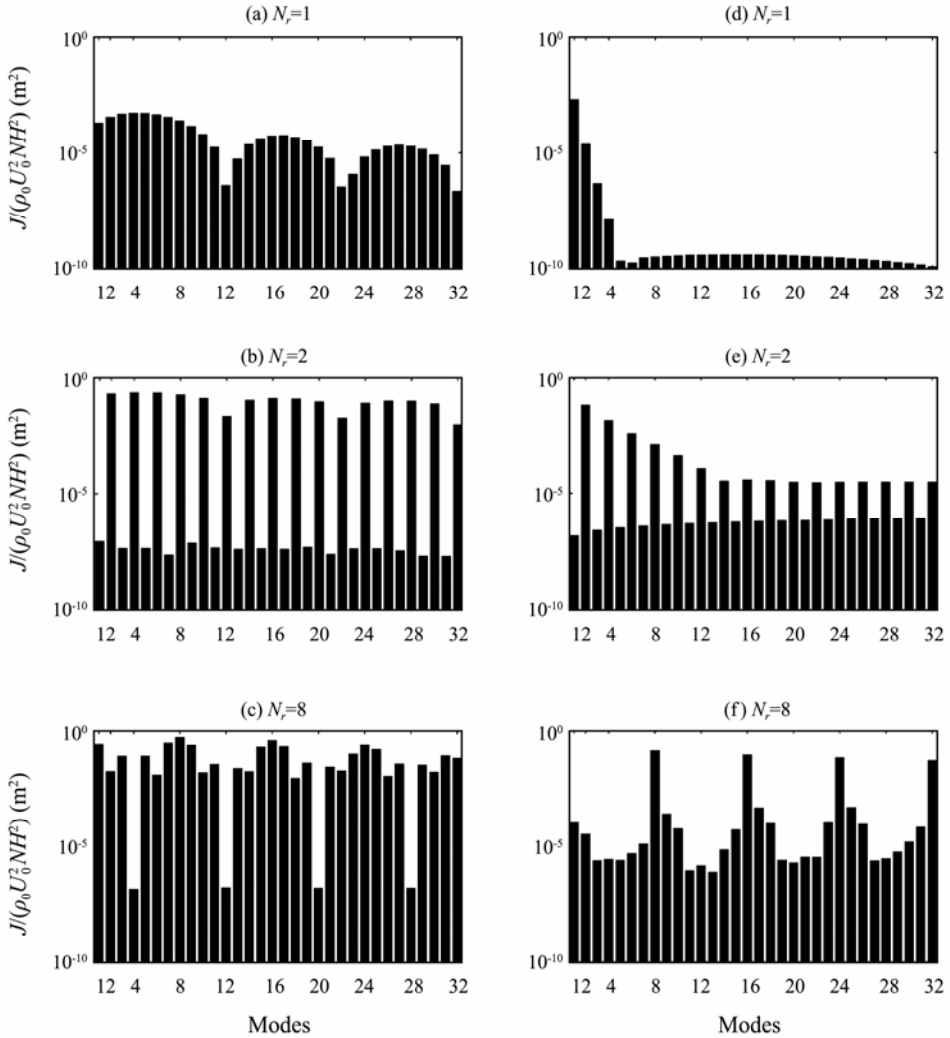

Fig.8 Energy flux in each mode calculated using the knife edge model (left) and the Green's function method (right).

bathymetry is larger than the mode-1 wavenumber. High-mode waves are easy to dissipate due to their short length scale, causing enhanced local mixing, as observed in the rough bathymetry in the Brazil Basin (Polzin *et al.*, 1997).

4 Nonlinear Model

Internal tides play an essential role in diapycnal mixing in the abyssal ocean (Garrett and Gerkema, 2007) via shear instability or nonlinear interaction forming smaller-scale breaking internal waves. The knife edge model and the Green's function method are both linear models and also assume no viscosity or diffusion. They cannot be directly used to describe dissipation caused by internal tides. Therefore, a regional ocean model, the MITgcm (Marshall *et al.*, 1997), is implemented to avoid these limitations of simplified linear models.

4.1 MITgcm and Configuration

The MITgcm setup is consistent with the linear models in a 2D *x*-*z* plane. The total depth is 1000 m, with a vertical resolution of 10 m. The horizontal resolution is 50 m in the center and gradually becomes coarse near the two lateral boundaries. The sinusoidal ridges are in the center of the domain, outside of which the bottom is flat. Tidal forcing is induced by imposing a vertically uniform tidal flow on each boundary. The tidal frequency is $\omega = 1.4\times 10^{-4}\,\mathrm{s}^{-1}$, corresponding to the M_2 tides. A rigid lid is used for the upper boundary to filter out fast-propagating barotropic gravity waves, which may cause unpredicted forcing in addition to tidal flow. Sponge layers are added at each lateral boundary to absorb all baroclinic signals propagating out of the domain. The earth's rotational effects are neglected ($f = 0$) to avoid parametric subharmonic instability. Hydrostatic approximation is applied to save computational time. The horizontal and vertical viscosity coefficients are set to $A_h = 1.0\times 10^{-3}\,\mathrm{m^2\,s^{-1}}$ and $A_v = 1.0\times 10^{-3}\,\mathrm{m^2\,s^{-1}}$, respectively. Sensitivity experiments reveal quantitatively similar results with non-hydrostatic runs and a relatively broad range of viscosity coefficients (Nikurashin and Legg, 2011). Other model parameters are shown in Table 2.

Table 2 Parameters in the MITgcm

Parameter	Notation	Value
Horizontal eddy viscosity coefficient	A_h	$1.0\times 10^{-3}\,\mathrm{m^2\,s^{-1}}$
Vertical eddy viscosity coefficient	A_v	$1.0\times 10^{-3}\,\mathrm{m^2\,s^{-1}}$
Horizontal diffusion coefficient	K_h	$1.0\times 10^{-5}\,\mathrm{m^2\,s^{-1}}$
Vertical diffusion coefficient	K_v	$1.0\times 10^{-5}\,\mathrm{m^2\,s^{-1}}$
Horizontal grid size	Δx	50–2696 m
Vertical grid size	Δz	10 m
Time step	Δt	2.5 s
Gravitational acceleration	g	$9.8\,\mathrm{m\,s^{-2}}$
Coriolis frequency	f	0
Buoyancy frequency	N	$5\times 10^{-3}\,\mathrm{s^{-1}}$
Reference density	ρ_0	$1000\,\mathrm{kg\,m^{-3}}$
Ridge height	h_0	100 m
Domain width	L	590 km
Domain depth	H	1000 m

4.2 Model Decomposition

Constant buoyancy frequency $N = 5\times 10^{-3}\,\mathrm{s^{-1}}$ is used. Thus, the vertical modal structure is sinusoidal. Modal decomposition is implemented every hour at the edge of the ridges through vertical integration of horizontal velocity u multiplied by the vertical structure function of each mode

$$A_m = \int_{-H}^{0} u \cos\frac{m\pi z}{H}\mathrm{d}z\,, \tag{17}$$

where A_m is a function of time. Each experiment runs for 20 tidal periods (T_{M2}), and the energy balance of modeled internal tides reaches a quasi-steady state after 10 tidal periods. For comparison with the linear models, the modal amplitude $<A_m>$ is calculated using a time average in the last 6 M_2 tidal periods

$$\langle A_m \rangle = \left[\frac{1}{5}\sum_{11T_{M2}}^{20T_{M2}} A_m^2\right]^{1/2}. \tag{18}$$

The energy flux in each mode is calculated using Eq. (12) and then compared with the linear model results calculated using the Green's function method for 8 and 16 ridges, shown in Fig.9. For the case with 8 ridges, the MITgcm results also show that energy concentrates on dominant modes, which are multiples of 8, consistent with the linear model. However, the energy in the dominant modes is considerably smaller than that in the linear model results due to dissipation. For the case with 16 ridges, if tidal forcing is weak ($U_0 = 0.01\,\mathrm{m\,s^{-1}}$), then energy flux concentrates on the dominant modes, which are multiples of 16. However, the energy concentration is not obvious for strong tidal forcing ($U_0 = 0.10\,\mathrm{m\,s^{-1}}$) probably because the vertical wavelength of mode-16 internal tides is $\lambda_{16} = 125$ m, comparable with the ridge height. The gen-

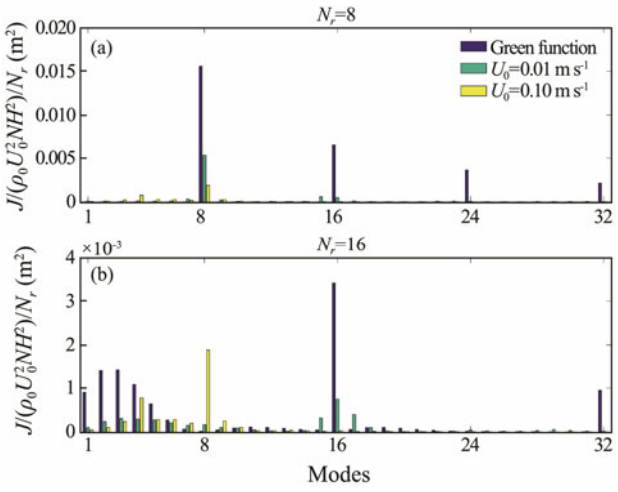

Fig.9 Normalized energy flux in each mode for 8 ridges (top) and 16 ridges (bottom). Blue represents the results calculated using the Green's function method. Green and yellow are obtained using the MITgcm with tidal forcing $U_0 = 0.01$ and $0.10\,\mathrm{m\,s^{-1}}$, respectively.

erated mode-16 internal tides are blocked to prevent them from escaping from the ridges. Interestingly, a large energy flux appears at mode 8. This inverse cascading probably results from nonlinear interaction between internal tides.

4.3 Energy Dissipation

The modelled dissipation over the ridges can be directly calculated using

$$D=\iint_A\left[A_z\left(\frac{\partial u}{\partial z}\right)^2+A_h\left(\frac{\partial u}{\partial x}\right)^2\right]\mathrm{d}A\,, \tag{19}$$

where A_z and A_h represent the vertical and horizontal viscosity coefficients. The dissipation are calculated every time step in the MITgcm and integrated every tidal period after the model reaches its quasi-steady state. High dissipation rates, as in the four examples shown in Fig.10, approximately coincide with the internal wave ray distribution obtained using the Green's function method (Fig.4) in deep water. This coincidence becomes less obvious if tidal forcing is strong (U_0=0.10 m s^{-1}), implying that nonlinear wave-wave interaction, which is sensitive to the velocity amplitudes, plays an important role in dissipation. The ray structure becomes blurred about 500 m above the ridges. Strong dissipation is especially obvious near the ridges through high-mode internal wave generation and reflection or scattering by topography. The latter effect is especially obvious if the internal wave ray reaches a supercritical slope.

In numerical experiments, dissipation includes the modelled dissipation and numerical dissipation. The total dissipation D can also be obtained using the difference between the conversion C and radiated energy flux $\boldsymbol{J}$

$$D=C-\nabla\cdot\boldsymbol{J}\,. \tag{20}$$

Sensitivity experiments reveal that, compared with the direct calculation using (19), this method can tolerate a relatively broad range of viscosity coefficients, because decreased modelled dissipation due to decreasing viscosity coefficients can be offset by increased numerical dissipation. Averaged dissipation in each ridge is shown in Fig.11 for different ridge number N_r and tidal forcing U_0. For small tidal forcing (U_0=0.01 m s^{-1}), the variation of dissipation follows a similar trend as the conversion rate predicted by the linear model (Fig.7). It reaches a maximum at N_r=8, in which constructive interference takes place between each ridge and a large amount of energy is converted from barotropic tides to internal tides. For large tidal forcing (U_0=0.01 m s^{-1}), the dissipation reaches a maximum at N_r=8 and then decreases monotonically. The model results show that, with increasing ridge number for N_r>8, the total conversion rate approximates a saturation but the radiated energy flux decreases. Therefore, the total dissipation increases at a relatively small rate and the averaged dissipation decreases.

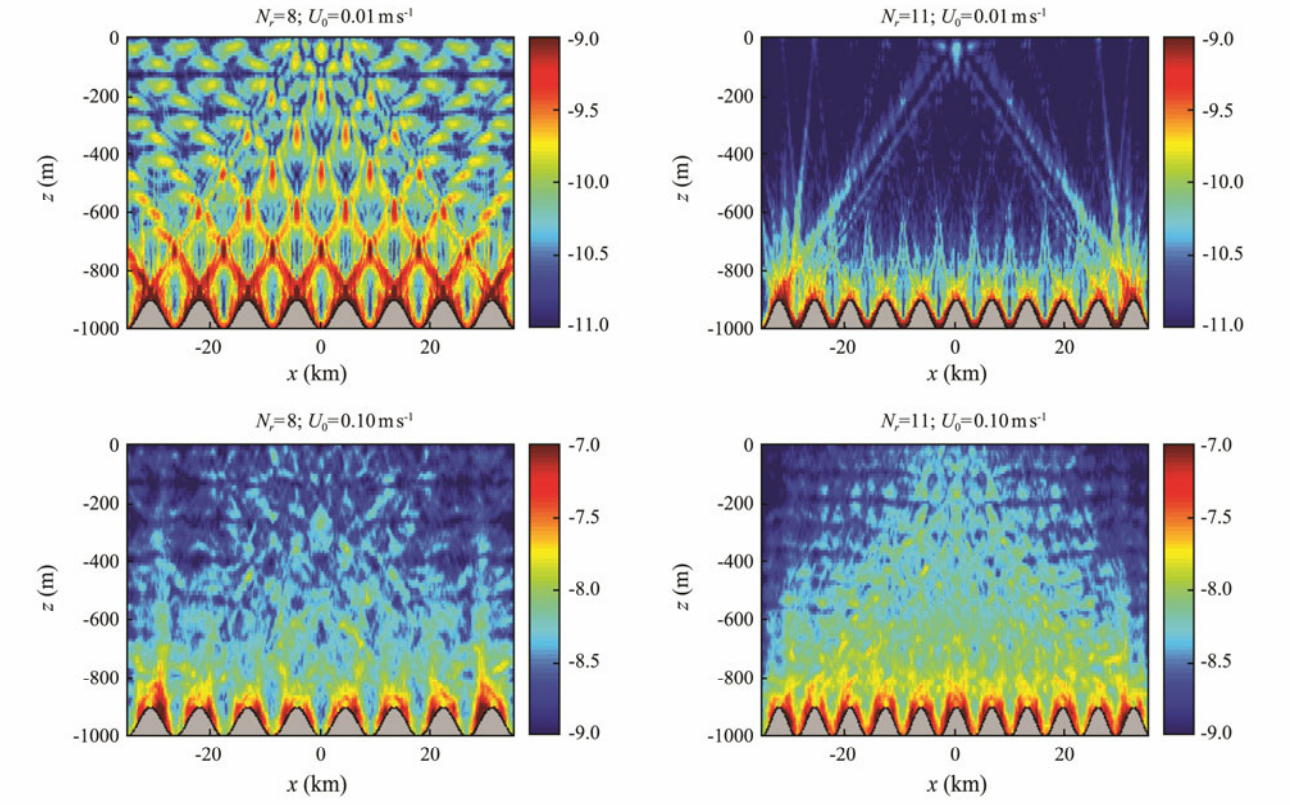

Fig.10 Time-averaged dissipation rate ($\log_{10}$ [W kg^{-1}]) calculated from the MITgcm within the 10th tidal period. The amplitude of barotropic tidal flow in the top two panels is 0.01 m s^{-1} with 8 (left) and 11 (right) sinusoidal ridges, respectively, and 0.10 m s^{-1} for the bottom two panels.

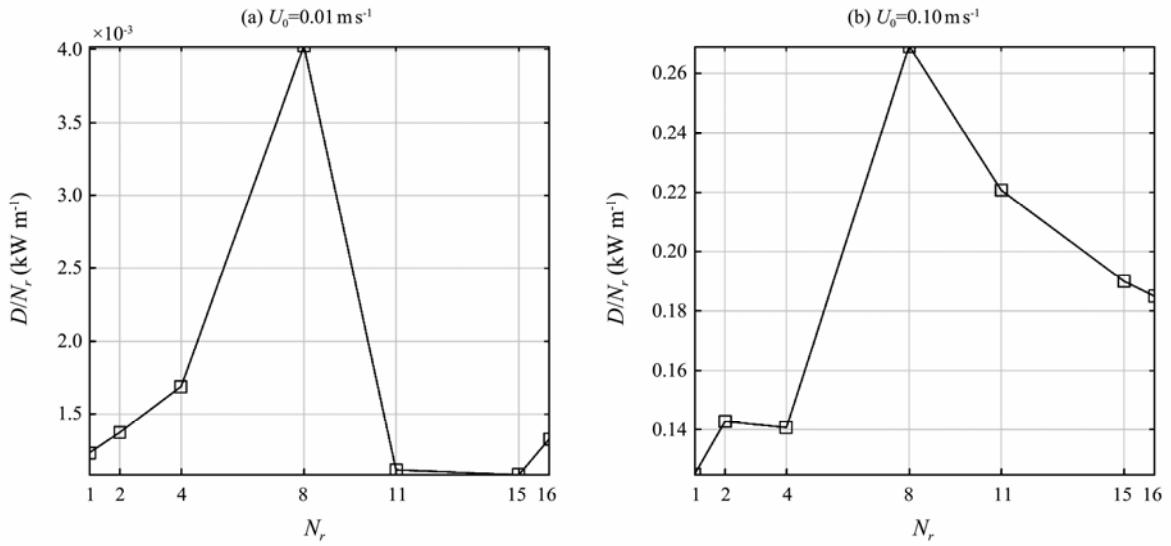

Fig.11 Averaged dissipation in each ridge (a) for the amplitude of tidal forcing $U_0=0.01\,\mathrm{m\,s^{-1}}$ and (b) for $U_0=0.10\,\mathrm{m\,s^{-1}}$.

5 Conclusions

The generation of internal tides from a rough sea floor is an important process that causes diapycnal mixing in the abyssal ocean, providing roughly half of the potential energy to maintain global stratification. Internal tide generation is first investigated using two linear models, in which the topography is represented by periodic knife edges and by sinusoidal ridges. In the models, the topographic height (100 m) is smaller than the total water depth (1000 m), imitating a rough sea floor in the abyssal ocean. The total length of the bottom topographic feature is one wavelength of mode-1 internal tides. The sharp shape of the knife edge is extremely supercritical. Therefore, the average energy flux by each knife edge is greater than that by each sinusoidal ridge. Interactions between internal wave rays emitted from each ridge may enhance or reduce the tidal conversion depending on their in-phase or out-of-phase interference. In addition, both linear models show that the energy flux concentrated on specific modes, with the mode numbers being multiples of the total number of knife edges or ridges, because of the power spectrum of the body force. High-mode internal waves dissipate quickly. This phenomenon implies that, in a real ocean, most of the energy of internal tides generated by rough topography dissipates locally and cannot escape.

A fully nonlinear numerical model that includes viscosity and diffusion is then implemented and compared with the linear model. In the nonlinear model, internal wave rays are emitted from ridges, showing a pattern similar to the linear model prediction. The rays propagate upwards and dissipate quickly. The ray structure becomes blurred ~500 m above the ridges due to dissipation. The distribution of dissipation rates coincides with the ray distribution, suggesting that nonlinear wave-wave interaction is a dominant mechanism for dissipation. Compared with the linear model, the energy flux in each mode is markedly reduced. Although we can observe that energy flux concentrates on modes whose mode number is a multiple of the ridge number, energy also disperses to other modes. An inverse cascade is observed especially for strong tidal forcing.

The linear and nonlinear models in this paper use idealized topography and stratification. The conclusions can provide some fundamental insights to the relationship between mixing and a rough sea floor. Low-mode internal tides can propagate away and high-mode internal tides are trapped locally; the latter is a major contributor to mixing. The efficiency of internal tide energy that is converted to local mixing is still an open question. Climate models use 30% following the guidelines given by St. Laurent and Garrett (2002). Apparently, this fixed value is not always true, but depends on tidal forcing and topographic features. For example, the model results in Fig.10 show varied efficiency of conversion from internal tides to dissipation. Understanding the mixing mechanism and then using the linear model as a reference to evaluate the conversion efficiency may be a feasible approach to developing a mixing ‘recipe’ in the abyssal ocean.

Acknowledgements

The helpful discussions with Drs. Samuel Kelly and John Huthnance are greatly appreciated. Comments and suggestions from two anonymous reviewers have greatly improved the manuscript. This work was supported by the Project of State Key Laboratory of Satellite Ocean Environment Dynamics, Second Institute of Oceanography (No. SOEDZZ1701), the Youth Visiting ‘Ocean-Star Scholarship’ of the State Key Laboratory of Satellite Ocean Environment Dynamics (No. QNHX1602) and National Key R&D Program of China (No. 2017YFC0305900). We gratefully acknowledge the support of NSFC-41576008 and CXZZ20140521161827690. Numerical computation is supported by the Special Program for Applied Research on Super Computation of the NSFC-Guangdong Joint Fund (No. U1501501).

References

Balmforth, N. J., and Peacock, T., 2009. Tidal conversion by supercritical topography. *Journal of Physical Oceanography*, **39**: 1965-1974.

Bell, T. H., 1975. Lee waves in stratified fluid with simple harmonic time dependence. *Journal of Fluid Mechanics*, **67**: 705-722.

Echeverri, P., and Peacock, T., 2010. Internal tide generation by arbitrary two-dimensional topography. *Journal of Fluid Mechanics*, **659**: 247-266.

Garrett, C., 2003. Internal tides and ocean mixing. *Science*, **301**: 1858-1859.

Garrett, C., and Gerkema, T., 2007. On the body-force term in internal-tide generation. *Journal of Physical Oceanography*, **37**: 2172-2175.

Garrett, C., and Kunze, E., 2007. Internal tide generation in the deep ocean. *Annual Review of Fluid Mechanics*, **39** (1): 57-87.

Kelly, S. M., and Nash, J. D., 2010. Internal-tide generation and destruction by shoaling internal tides. *Geophysical Research Letters*, **37**: L23611, DOI: 10.1029/2010GL045598.

Kelly, S. M., Jones, N. L., and Nash, J. D., 2013. A coupled model for Laplace's tidal equations in a fluid with one horizontal dimension and variable depth. *Journal of Physical Oceanography*, **43**: 1780-1797.

Klymak, J. M., Buijsman, M., Legg, S., and Pinkel, R., 2013. Parameterizing surface and internal tide scattering and breaking on supercritical topography: The one- and two-ridge cases. *Journal of Physical Oceanography*, **43**: 1380-1397.

Marshall, J., Adcroft, A., Hill, C., Perelman, L., and Heisey, C., 1997. A finite-volume, incompressible Navier Stokes model for studies of the ocean on parallel computers. *Journal of Geophysical Research Atmospheres*, **102** (C3): 5753-5766.

Muller, C., and Bühler, O., 2009. Saturation of the internal tides and induced mixing in the abyssal ocean. *Journal of Physical Oceanography*, **39**: 2077-2096.

Nikurashin, M., and Legg, S., 2011. A mechanism for local dissipation of internal tides generated at rough topography. *Journal of Physical Oceanography*, **41**: 378-395.

Pétrélis, F., Smith, S. L., and Young, W. R., 2006. Tidal conversion at a submarine ridge. *Journal of Physical Oceanography*, **36**: 1053-1071.

Polzin, K. L., 2004. Idealized solutions for the energy balance of the finescale internal wave field. *Journal of Physical Oceanography*, **34**: 231-246.

Polzin, K. L., 2009. An abyssal recipe. *Ocean Modelling*, **30**: 298-309.

Polzin, K. L., Toole, J. M., Ledwell, J. R., and Schmitt, R. W., 1997. Spatial variability of turbulent mixing in the abyssal ocean. *Science*, **276**: 93-96.

Sarkar, S., and Scotti, A., 2017. From topographic internal gravity waves to turbulence. *Annual Review of Fluid Mechanics*, **49**: 195-220.

St. Laurent, L., and Garrett, C., 2002. The role of internal tides in mixing the deep ocean. *Journal of Physical Oceanography*, **32**: 2882-2899.

St. Laurent, L., Stringer, S., Garrett, C., and Perrault-Joncas, D., 2003. The generation of internal tides at abrupt topography. *Deep Sea Research Part I Oceanographic Research Papers*, **50** (8): 987-1003.

(Edited by Xie Jun)